Supplementary Material
Static Promise versus Dynamic Reality in a Z-Scheme Photocatalyst: Nonadiabatic Dynamics Reveal a Charge-Separation Bottleneck in $MoSi_2P_4/WTe_2$

Mengran Qin[1], Xiangjie Chen[1], Xiefei Song[1,2], Jifan Wan[1], Yao He*[1], and Kai Xiong†[3]

[1]Department of Physics, Yunnan University
[2]College of Physics and Information Engineering, Zhaotong University
[3]Materials Genome Institute, School of Materials and Energy, Yunnan University

1 The geometrical configurations and electronic properties of the monolayers and heterostructures

Material	Property	This work	Literature value
Reference			
$MoSi_2P_4$	Lattice constant (Å)	3.45	3.47 [1, 2]
	HSE06 bandgap (eV)	0.99	1.18 [1], 0.99 [2]
WTe_2	Lattice constant (Å)	3.52	3.55 [3], 3.56 [4]
	HSE06 bandgap (eV)	1.60	1.58 [3], 1.63 [4]

Table S1. Comparison of calculated lattice constants and bandgap values with previous literature

*Corresponding author
†Corresponding author

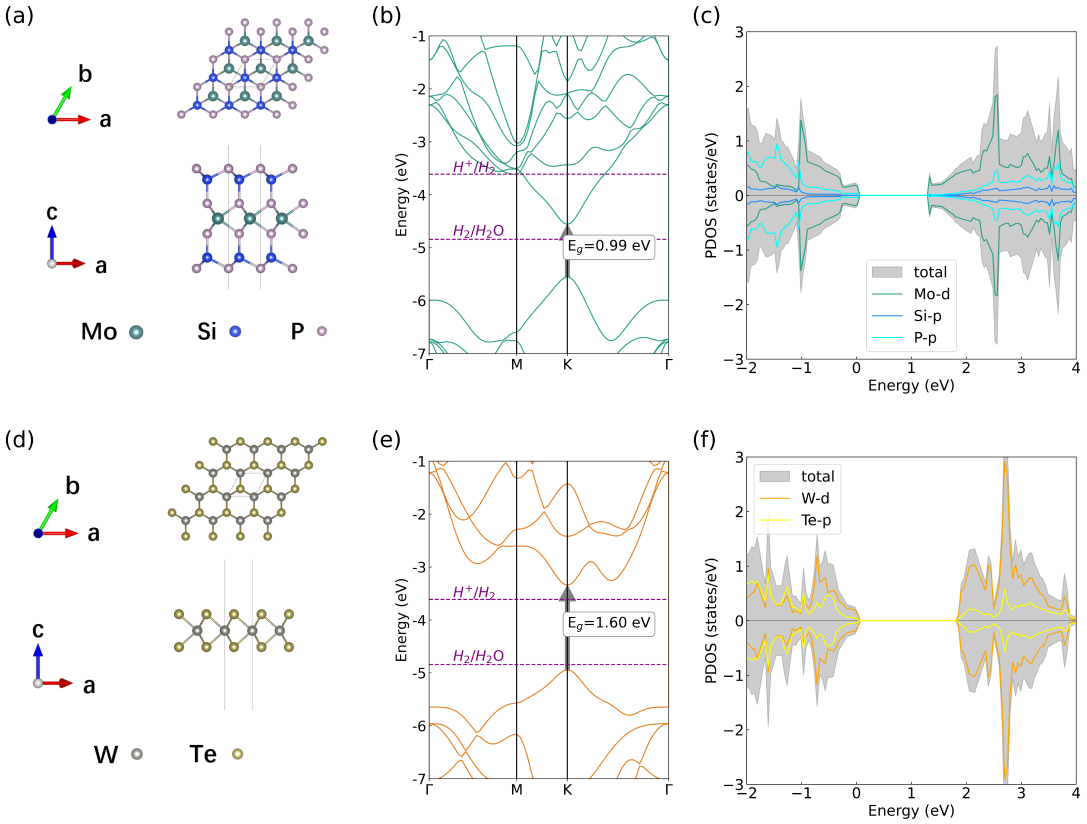

Fig. S1. Top and side views of (a,d), band structures of (b,e), and projected density of states of (c,f) for $MoSi_2P_4$ and WTe_2 monolayers. The dashed purple lines indicate water splitting redox potentials at pH = 14.

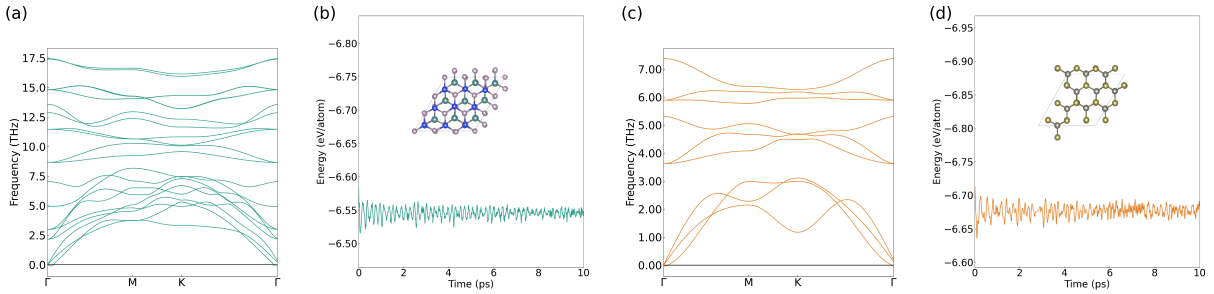

Fig. S2. Phonon spectra and AIMD simulation results for (a,c) $MoSi_2P_4$ and (b,d) WTe_2 monolayers. Panels (a,b) display the phonon dispersion relations, while (c,d) show the AIMD trajectories at 300 K. The illustration in (b) and (d) shows the post-AIMD structure.

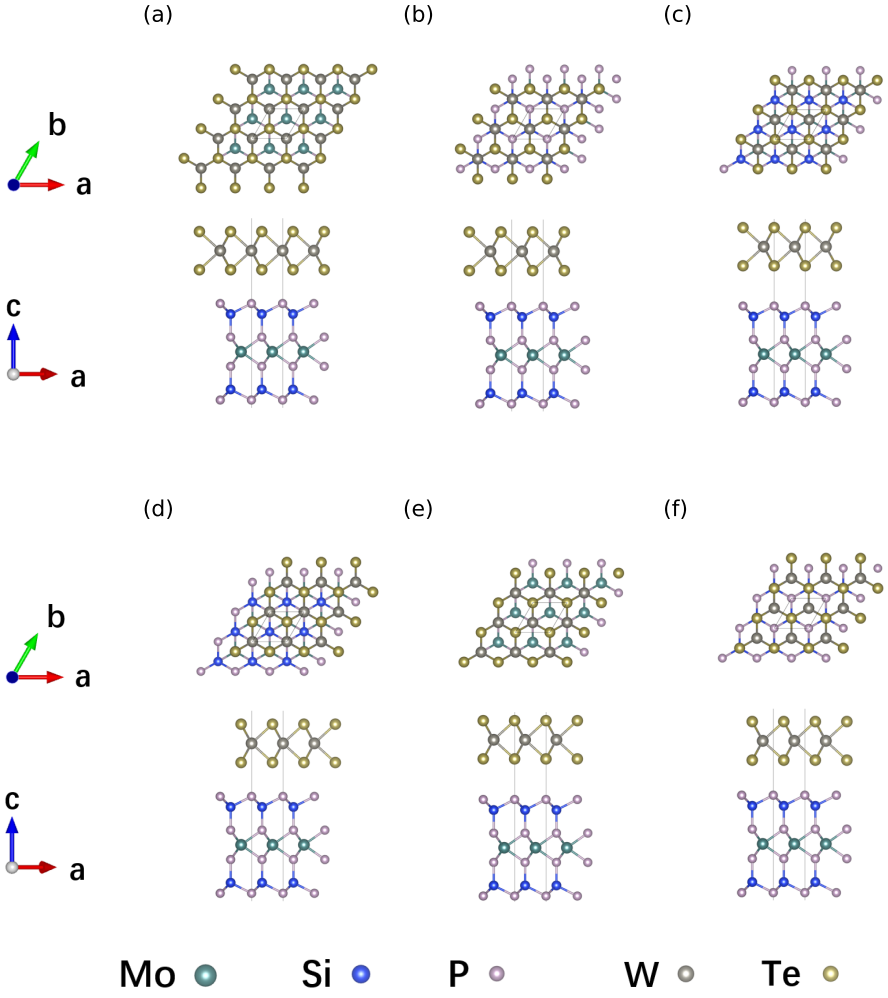

Fig. S3. Top and side views of the $MoSi_2P_4/WTe_2$ heterostructure for (a) W_P_i configuration, (b) W_Si_i configuration, (c) W_Mo_i configuration, (d) W_P_ii configuration, (e) W_Si_ii configuration, and (f) W_Mo_ii configuration.

Structure	a (Å)	d (Å)	E_F (eV)	E_B (meV/Å^2)
W_P_i $MoSi_2P_4/WTe_2$	3.47	3.26	-278.30	-23.11
W_P_ii $MoSi_2P_4/WTe_2$	3.47	3.26	-275.95	-22.92
W_Si_i $MoSi_2P_4/WTe_2$	3.47	3.41	-243.33	-20.21
W_Si_ii $MoSi_2P_4/WTe_2$	3.47	3.92	-178.85	-14.85
W_Mo_i $MoSi_2P_4/WTe_2$	3.47	3.90	-181.77	-15.10
W_Mo_ii $MoSi_2P_4/WTe_2$	3.47	3.35	-257.61	-21.39

Table S2. Lattice parameters (a), interlayer distance (d), formation energy (E_F), and binding energy (E_B) for the considered $MoSi_2P_4/WTe_2$ configurations.

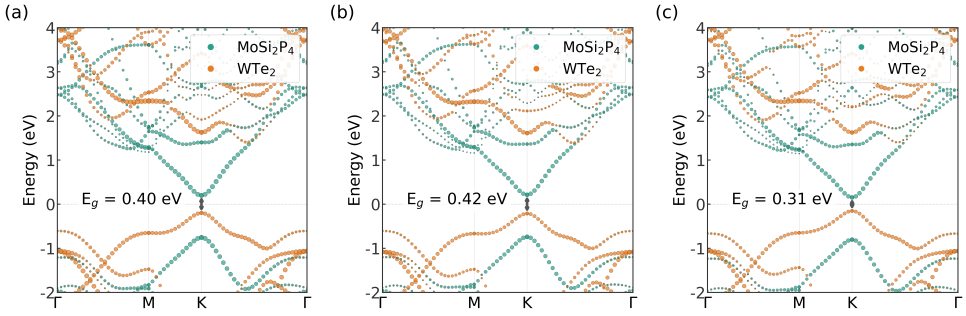

Fig. S4. Projected band structures of the $MoSi_2P_4/WTe_2$ heterostructure for the three stacking configurations: (a) W_P_i, (b) W_P_ii, and (c) W_Mo_ii.

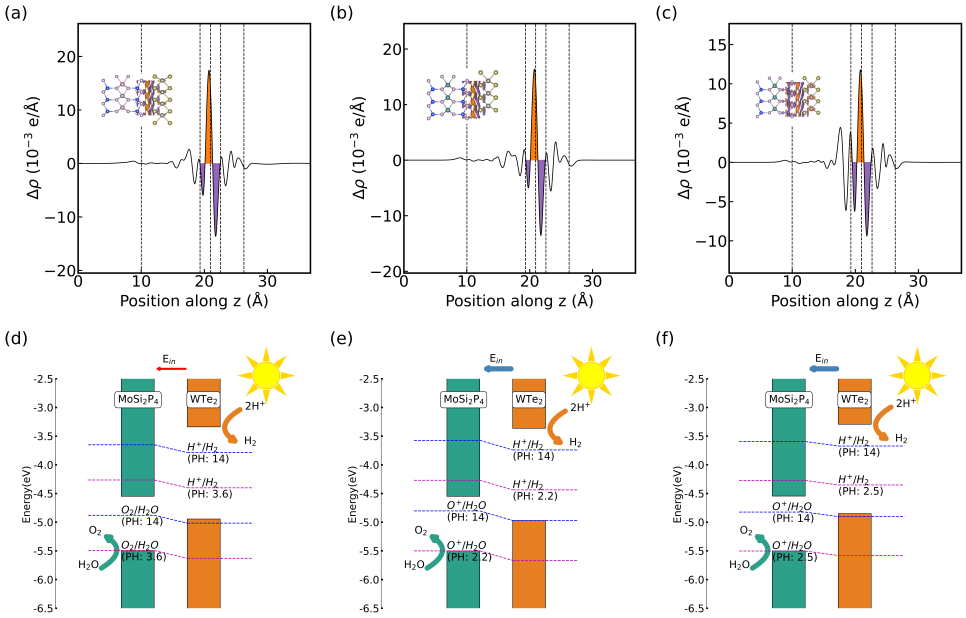

Fig. S5. Plane-integrated charge density difference ($\Delta\rho$) along the z-direction (a-c) and band edge alignment (d-f) for the three considered configurations (W_P_i, W_P_ii, and W_Mo_ii) of the $MoSi_2P_4/WTe_2$ heterostructure. The orange and purple regions in (a-c) represent electron accumulation and depletion, respectively.

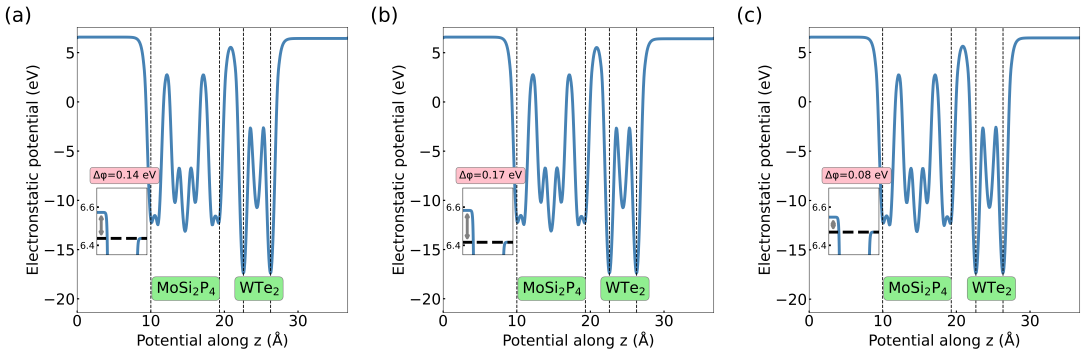

Fig. S6. Calculated electrostatic potential of the $MoSi_2P_4/WTe_2$ heterostructure for the three interfacial configurations: (a) W_P_i, (b) W_P_ii, and (c) W_Mo_ii.

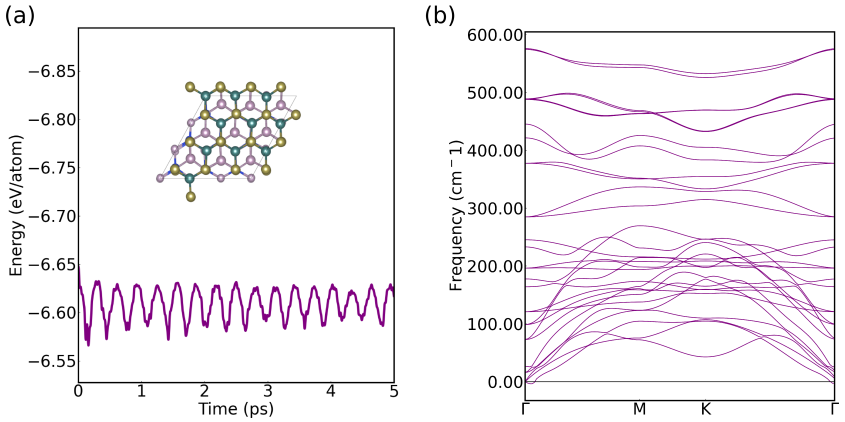

Fig. S7. (a) AIMD simulation and (b) phonon dispersion of the W_P_i-configured $MoSi_2P_4/WTe_2$ heterostructure. The illustration in (a) shows the structure after AIMD.

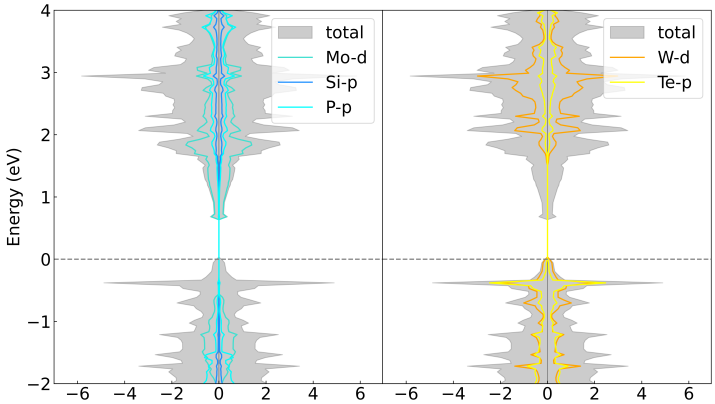

Fig. S8. Projected density of states of the W_P_i-configured $MoSi_2P_4/WTe_2$ heterostructure.

2 Calculational details for the solar-to-hydrogen conversion efficiency and the optical properties

The solar-to-hydrogen conversion efficiency (η_{STH}), defined as the product of the light absorption efficiency (η_{abs}) and carrier utilization efficiency (η_{cu}), quantifies the overall photocatalytic hydrogen production performance. Here η_{abs} measures the fraction of incident solar radiation absorbed above the photocatalyst's bandgap, while η_{cu} evaluates the effectiveness of photogenerated charge carriers in driving redox reactions. This combined metric comprehensively assesses the system's ability to harness solar energy through three critical processes: (1) photon absorption, (2) charge separation/transport, and (3) surface catalytic reactions for water splitting. We calculated η_{STH}, η_{abs}, and η_{cu} based on the following formula [5] [6]:

$$\eta_{\mathrm{STH}} = \eta_{\mathrm{abs}} \times \eta_{\mathrm{cu}} \tag{1}$$

$$\eta_{\mathrm{abs}} = \frac{\int_{E_g}^{\infty} P(\hbar\omega)\,\mathrm{d}(\hbar\omega)}{\int_{0}^{\infty} P(\hbar\omega)\,\mathrm{d}(\hbar\omega)} \tag{2}$$

$$\eta_{\mathrm{cu}} = 0.5 \times \frac{\Delta G \int_{E}^{\infty} \frac{P(\hbar\omega)}{\hbar\omega}\,\mathrm{d}(\hbar\omega)}{\int_{E_g}^{\infty} P(\hbar\omega)\,\mathrm{d}(\hbar\omega)} \tag{3}$$

$$E = \begin{cases} E_g & \chi(\mathrm{H_2}) \geq 0.2 \text{ and } \chi(\mathrm{O_2}) \geq 0.6 \\ E_g + 0.2 - \chi(\mathrm{H_2}) & \chi(\mathrm{H_2}) < 0.2 \text{ and } \chi(\mathrm{O_2}) \geq 0.6 \\ E_g + 0.6 - \chi(\mathrm{O_2}) & \chi(\mathrm{H_2}) \geq 0.2 \text{ and } \chi(\mathrm{O_2}) < 0.6 \\ E_g + 0.8 - \chi(\mathrm{H_2}) - \chi(\mathrm{O_2}) & \chi(\mathrm{H_2}) < 0.2 \text{ and } \chi(\mathrm{O_2}) < 0.6 \end{cases} \tag{4}$$

where $P(\hbar\omega)$ represents the AM1.5G solar spectral irradiance at photon energy $\hbar\omega$, E_g denotes the larger bandgap among the constituent monolayer materials, $\chi(\mathrm{H_2})$ and $\chi(\mathrm{O_2})$ are the hydrogen and oxygen evolution reaction overpotentials respectively, ΔG is the thermodynamic potential (1.23 eV) required for water splitting, and E corresponds to the actual utilizable photon energy for the water splitting process. The factor of 0.5 accounts for the 50% theoretical apparent quantum yield in Z-scheme photocatalytic water splitting, considering electron-hole recombination.

Work function differences ($\Delta\phi$) also play a critical role in modulating the photocatalytic water splitting activity. We therefore evaluate the corrected solar-to-hydrogen efficiency (η'_{STH}): [7]

$$\eta'_{\mathrm{STH}} = \eta_{\mathrm{STH}} \times \frac{\int_{0}^{\infty} P(\hbar\omega) d(\hbar\omega)}{\int_{0}^{\infty} P(\hbar\omega) d(\hbar\omega) + \Delta\phi \int_{E_g}^{\infty} \frac{P(\hbar\omega)}{\hbar\omega}\, d(\hbar\omega)}$$

Strain (%)	$\chi(\mathbf{H_2})$ **(eV)**	$\chi(\mathbf{O_2})$ **(eV)**	$E_g(\mathbf{MoSi_2P_4})$ **(eV)**	$E_g(\mathbf{WTe_2})$ **(eV)**	$\Delta\phi$ **(eV)**	$\eta_{\mathbf{abs}}$ (%)	$\eta_{\mathbf{cu}}$ (%)	$\eta_{\mathbf{STH}}$ (%)	$\eta'_{\mathbf{STH}}$ (%)
-6	0.31	0.39	1.35	1.47	0.17	63.27	22.54	14.16	13.55
-5	0.26	0.51	1.27	1.59	0.16	56.53	25.07	14.17	13.59
-4	0.53	0.32	1.18	1.67	0.16	52.59	18.31	9.63	9.29
-3	0.41	0.51	1.11	1.66	0.15	53.08	24.35	12.92	12.48
-2	0.45	0.54	1.05	1.66	0.15	53.33	25.35	13.52	13.06
-1	0.50	0.56	0.99	1.65	0.14	53.70	25.98	13.95	13.50
0	0.31	0.81	0.94	1.64	0.14	54.20	27.59	14.95	14.47
1	0.45	0.72	0.89	1.63	0.13	54.82	27.70	15.18	14.70
2	0.34	0.84	0.85	1.57	0.13	57.46	28.19	16.20	15.66
3	0.20	0.91	0.81	1.47	0.13	62.87	29.23	18.38	17.69
4	0.05	0.91	0.78	1.37	0.13	68.47	25.29	17.32	16.58

Table S3. Overpotentials, η_{STH} and η'_{STH} of the $MoSi_2P_4/WTe_2$ heterostructure based on different biaxial strains at PH=14

The optical absorption coefficient $\alpha(\omega)$ is derived from the complex dielectric function $\varepsilon(\omega) = \varepsilon_1(\omega) + i\varepsilon_2(\omega)$ as follows [9, 10]:

$$\alpha(\omega) = \sqrt{2}\omega\sqrt{\sqrt{\varepsilon_1^2(\omega) + \varepsilon_2^2(\omega)} - \varepsilon_1(\omega)} \tag{5}$$

The imaginary component $\varepsilon_2(\omega)$ of the dielectric function, is given by [11]:

$$\varepsilon_2(\omega) = \frac{4\pi^2}{m^2\omega^2}\sum_{c,v}\int_{\mathrm{BZ}}\frac{2}{(2\pi)^3}|\mathbf{M}_{cv}(\mathbf{k})|^2\delta(\varepsilon_{c\mathbf{k}} - \varepsilon_{v\mathbf{k}} - \hbar\omega)\,\mathrm{d}^3\mathbf{k} \tag{6}$$

where $|\mathbf{M}_{cv}(\mathbf{k})|^2$ denotes the momentum matrix element between conduction (c) and valence (v) band states at wavevector $\mathbf{k}$, and the integration spans the entire Brillouin zone (BZ). The real component $\varepsilon_r(\omega)$ is obtained through the Kramers-Kronig transformation of $\varepsilon_i(\omega)$ [12,13], ensuring the causality-constrained relationship between both components.

3 Calculation Procedures of Gibbs Free Energy for HER and OER Pathways

The Gibbs free energy change ΔG for each elementary step is computed using the established computational hydrogen electrode (CHE) model [14], as described by the equation:

$$\Delta G = \Delta E + \Delta E_{ZPE} - T\Delta S - U$$

Here, ΔE is the change in reaction energy. ΔE_{ZPE} denotes the difference in the zero-point energy. The ΔS is the entropy difference. The system temperature T is set to be 298.15 K. The U is the external potential for photogenerated electrons. This approach allows for a systematic evaluation of the thermodynamic feasibility of both the hydrogen evolution reaction and oxygen evolution reaction on the catalytic surface.

For the HER, the Gibbs free energy barrier for hydrogen adsorption, denoted as ΔG_{H^*}, is calculated using the following approach:

$$\Delta G_{H^*} = G(H^*) - G(*) - 0.5G(H_2) - U_e$$

For the OER with O_2 as the final product, there are three possible reaction pathways, and the corresponding calculation formulas are as follows: [15] [16]

OER-I:

$$\Delta G_{OH^*} = G(OH^*) - G(*) + 0.5G(H_2) - G(H_2O) - U_h$$

$$\Delta G_{O^*} = G(O^*) - G(OH^*) + 0.5G(H_2) - U_h$$

$$\Delta G_{OOH^*} = G(OOH^*) - G(O^*) + 0.5G(H_2) - G(H_2O) - U_h$$

OER-II:

$$\Delta G_{OH^*} = G(OH^*) - G(*) + 0.5G(H_2) - G(H_2O) - U_h$$

$$\Delta G_{O^*} = G(O^*) - G(OH^*) + 0.5G(H_2) - U_h$$

$$\Delta G_{O^*OH^*} = G(O^*OH^*) - G(O^*) + 0.5G(H_2) - G(H_2O) - U_h$$

$$\Delta G_{O^*O^*} = G(O^*O^*) - G(O^*OH^*) + 0.5G(H_2) - U_h$$

$$\Delta G_{OO^*} = G(OO^*) - G(O^*O^*) - U_h$$

OER-III:

$$\Delta G_{OH^*} = G(OH^*) - G(*) + 0.5G(H_2) - G(H_2O) - U_h$$

$$\Delta G_{HOOH^*} = G(HOOH^*) - G(OH^*) + 0.5G(H_2) - G(H_2O) - U_h$$

$$\Delta G_{OOH^*} = G(OOH^*) - G(HOOH^*) + 0.5G(H_2) - U_h$$

where * denotes an adsorption site on the catalyst surface.

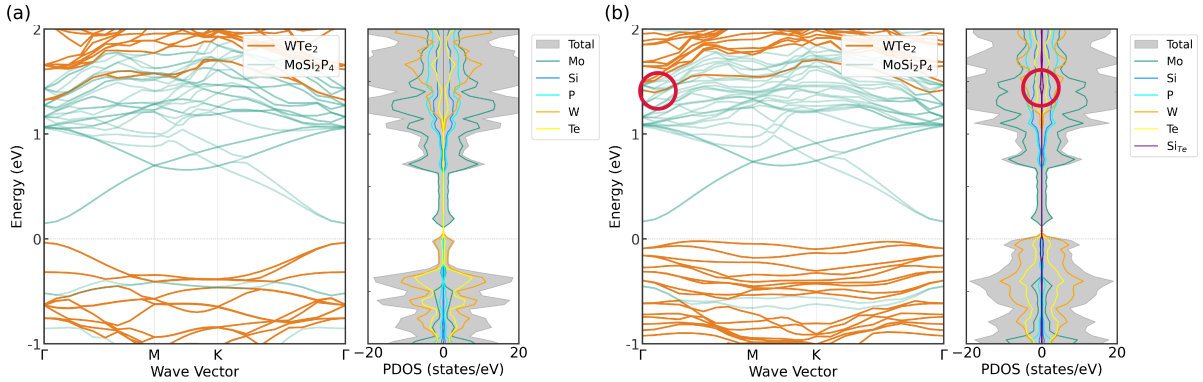

Fig. S9. Electronic band structures and projected density of states (PDOS) of the heterostructures. (a) The pristine 3×3×1 $MoSi_2N_4/WTe_2$ heterostructure. (b) The 3×3×1 Si-doped $MoSi_2N_4/WTe_2$ heterostructure.

4 k-Space Folding: From Primitive Cell to Supercell

To understand the physical origin of the features near the Γ point in the supercell band structure, this supplementary information briefly reviews the principle of k-space folding from the primitive cell to the supercell.

The $MoSi_2N_4/WTe_2$ heterostructure investigated in this work possesses a hexagonal lattice structure, with an interaxial angle of 60° in its primitive cell. Let the real-space basis vectors of the primitive cell be $\mathbf{a}_1$, $\mathbf{a}_2$ (lying in the 2D plane), and $\mathbf{a}_3$ (perpendicular to the plane). The real-space basis vectors of its primitive cell can be chosen as (where a and c is the lattice constant):

$$\begin{aligned} \mathbf{a}_1 &= a\,(1,0,0)\,, \\ \mathbf{a}_2 &= a\left(\frac{1}{2},\frac{\sqrt{3}}{2},0\right), \\ \mathbf{a}_3 &= c\,(0,0,1)\,. \end{aligned} \tag{7}$$

The corresponding reciprocal-space basis vectors $\mathbf{b}_i$, defined by the relation $\mathbf{a}_i \cdot \mathbf{b}_j = 2\pi\delta_{ij}$, are:

$$\begin{aligned} \mathbf{b}_1 &= \frac{2\pi}{a}\left(1,-\frac{1}{\sqrt{3}},0\right), \\ \mathbf{b}_2 &= \frac{2\pi}{a}\left(0,\frac{2}{\sqrt{3}},0\right), \\ \mathbf{b}_3 &= \frac{2\pi}{c}\,(0,0,1)\,. \end{aligned} \tag{8}$$

The first Brillouin zone is defined as the Wigner-Seitz cell in the reciprocal space. Formally, it is the primitive cell of the reciprocal lattice constructed by drawing the perpendicular bisectors (Bragg planes) of the reciprocal lattice vectors connecting the

origin to its nearest neighbors.

For the hexagonal lattice defined by $\mathbf{b}_1$ and $\mathbf{b}_2$ above, this construction results in a first Brillouin zone with the shape of a regular hexagon. Its high-symmetry points are shown in Fig. S10, primarily including the Brillouin zone center Γ point, the hexagon vertices K points, and the edge midpoints M points. The coordinates of these points in the reciprocal space basis are:

$$\begin{aligned} \Gamma &= (0, 0, 0), \\ K &= \left(\frac{1}{3}, \frac{1}{3}, 0\right), \\ M &= \left(0, \frac{1}{2}, 0\right). \end{aligned} \tag{9}$$

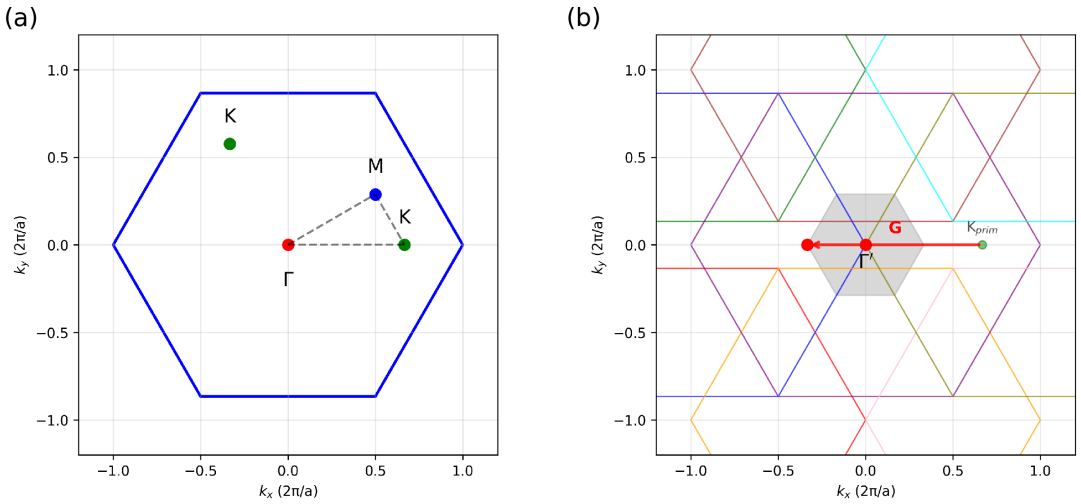

Fig. S10. (a) The first Brillouin zone of the primitive cell for the hexagonal lattice and its high-symmetry points. (b) The folded zone (grey hexagon) corresponding to the $3 \times 3 \times 1$ supercell. The Brillouin zone of the primitive cell is partitioned into 9 smaller regions and translated into the folded zone. The primitive cell's K point (red) is mapped to the supercell's Γ point by subtracting a reciprocal lattice vector $\mathbf{G}$.

We constructed a $3\times3\times1$ supercell. This transformation in real space can be described by the matrix $\mathbf{S}$:

$$\mathbf{S} = \begin{pmatrix} 3 & 0 & 0 \\ 0 & 3 & 0 \\ 0 & 0 & 1 \end{pmatrix} \tag{10}$$

The relationship between the real-space basis vectors $\mathbf{A}_i$ of the supercell and the primitive cell basis vectors $\mathbf{a}_i$ is:

$$\mathbf{A}_i = \sum_j S_{ij} \mathbf{a}_j \tag{11}$$

According to the reciprocal relationship, the reciprocal-space basis vectors $\mathbf{B}_i$ of the su-

percell and the primitive cell basis vectors $\mathbf{b}_i$ satisfy:

$$\mathbf{B} = (\mathbf{S}^{-1})^{\mathrm{T}} \cdot \mathbf{b} \tag{12}$$

where $(\mathbf{S}^{-1})^{\mathrm{T}}$ is the inverse transpose of the real-space transformation matrix $\mathbf{S}$. For the $3 \times 3 \times 1$ supercell:

$$(\mathbf{S}^{-1})^{\mathrm{T}} = \begin{pmatrix} \frac{1}{3} & 0 & 0 \\ 0 & \frac{1}{3} & 0 \\ 0 & 0 & 1 \end{pmatrix} \tag{13}$$

This implies that the reciprocal lattice vectors of the supercell are "compressed" to one-third of those of the primitive cell. Consequently, the area of the first Brillouin zone of the supercell (known as the folded zone) is 1/9 that of the primitive cell's first Brillouin zone, as visually demonstrated by the relative sizes of the hexagonal zones in Fig. S10(b).

The folding in k-space can be understood by the following relation, a fundamental concept in solid state physics [17]: any two wave vectors $\mathbf{k}$ and $\mathbf{k}'$ of the primitive cell are equivalent in the supercell band calculation if they satisfy:

$$\mathbf{k}' = \mathbf{k} + \mathbf{G}_{\mathrm{super}} \tag{14}$$

where $\mathbf{G}_{\mathrm{super}}$ is any reciprocal lattice vector of the supercell.

Specifically for this system, the coordinates of the primitive cell's K point are $\mathbf{k}_K = (\frac{1}{3}, \frac{1}{3}, 0)$ (in fractional coordinates). One can find a supercell reciprocal lattice vector $\mathbf{G} = (1, 0, 0)$ such that:

$$\mathbf{k}_K - \mathbf{G} = (\frac{1}{3}, \frac{1}{3}, 0) - (1, 0, 0) = (-\frac{2}{3}, \frac{1}{3}, 0) \tag{15}$$

This vector is equivalent to the Γ point within the folded zone of the supercell. Therefore, the electronic states of the primitive cell at the K point will appear at the Γ point in the supercell calculation.

5 Calculational detail of the NAMD simulation

During the nonadiabatic coupling (NAC) calculations and nonadiabatic molecular dynamics (NAMD) simulations, only the Γ-point Kohn-Sham orbitals of the supercell were computed. The simulations investigated carrier transfer time, energy relaxation in electron and hole transfer processes, as well as electron-hole recombination. The autocorrelation functions (ACF) were evaluated, and the corresponding spectral densities were obtained via Fourier transform. [18, 19]

The fluctuations of the energy gap are characterized by the autocorrelation function, defined as:

$$C(t) = \frac{\langle \delta U(t) \delta U(t_0) \rangle_T}{\langle (\delta U(t_0))^2 \rangle_T} = \frac{\mathcal{C}_{\mathrm{un}}(t)}{\langle \Delta E^2(0) \rangle_T}, \tag{16}$$

where $\mathcal{C}_{\mathrm{un}}(t)$ is the unnormalized ACF, $C(t)$ denotes the normalized ACF, t_0 represents different initial time origins in the statistical averaging process, and $\delta U(t)$ is the deviation of the energy gap from its average value, given by:

$$\delta U(t) = \Delta E_{ij}\big(\mathbf{R}(t)\big) - \langle \Delta E_{ij}\big(\mathbf{R}(t)\big) \rangle_T, \tag{17}$$

with ΔE_{ij} being the energy difference between states i and j, and $\mathbf{R}(t)$ determined through quantum forces.

The spectral density $I(\omega)$ was calculated through the Fourier transform of the normalized ACF:

$$I(\omega) = \left| \frac{1}{\sqrt{2\pi}} \int_{-\infty}^{+\infty} dt \; e^{-i\omega t} C(t) \right|^2 \tag{18}$$

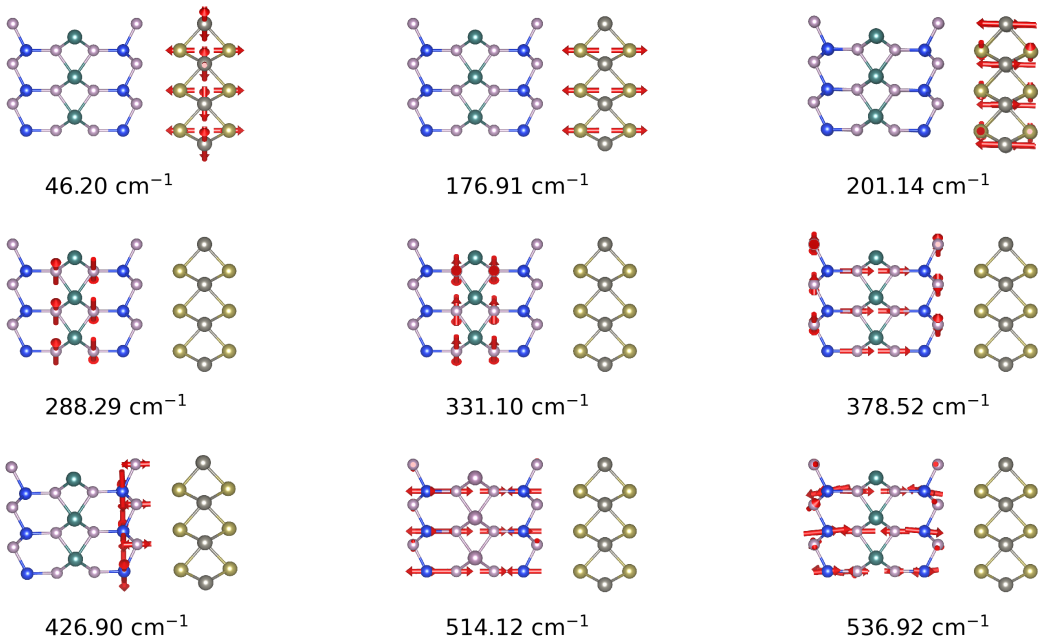

Fig. S11. Calculated vibrational modes of the $MoSi_2P_4/WTe_2$ heterostructure.

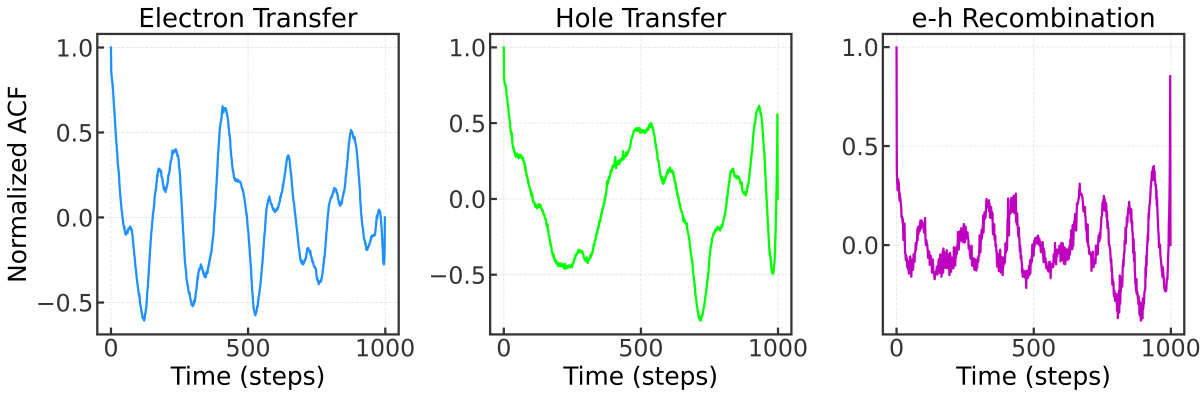

Fig. S12. Normalized energy-gap fluctuation autocorrelation function of the $MoSi_2P_4/WTe_2$ heterostructure.

References

[1] Trilokchand L Kumavat, Radha N Somaiya, and Yogesh Sonvane. Strain modulated optical properties of $MoSi_2P_4$ monolayer – insights from DFT. *Physica Scripta*, 99(6):065930, 2024.

[2] Xianghe Liu, Hua Zhang, Zhixiong Yang, Zhenhua Zhang, Xiang Fan, and Huan Liu. Structure and electronic properties of $MoSi_2P_4$ monolayer. *Physics Letters A*, 420:127751, 2021.

[3] Changxin Wan, Wei Yan, Chunsheng Liu, Lan Meng, and Xiaohong Yan. First-principles study of direct Z-scheme GaS/WTe_2 van der Waals heterostructure as photocatalyst for water splitting. *Physica B: Condensed Matter*, 682:415882, 2024.

[4] Yi-Dan Feng, Yan Zhang, Dou-Dou Cheng, Ying-Ying Jia, Hui-Ru Zhu, and Li Duan. Theoretical design of a direct Z-scheme WTe_2/PtS_2 van der Waals heterostructure for high-efficiency photocatalytic overall water-splitting. *Molecular Catalysis*, 585:115368, 2025.

[5] Cen-Feng Fu, Jiuyu Sun, Qiquan Luo, Xingxing Li, Wei Hu, and Jinlong Yang. Intrinsic Electric Fields in Two-dimensional Materials Boost the Solar-to-Hydrogen Efficiency for Photocatalytic Water Splitting. *Nano Letters*, 18(10):6312–6317, 2018.

[6] Y. Fan, J. Wang, M. Zhao. Spontaneous full photocatalytic water splitting on 2D MoSe2/SnSe2 and WSe2/SnSe2 vdW heterostructures. *Nanoscale*, 11:14836–14843, 2019.

[7] Xiao-Ting Li, Chuan-Lu Yang, Wen-Kai Zhao, Yu-Liang Liu. Photocatalytic Z-scheme overall water splitting for hydrogen generation with Sc_2CCl_2/ML (ML = $MoTe_2$, Hf_2CO_2) heterostructures. *Int. J. Hydrogen Energy*, 59: 214–223, 2024.

[8] Mark S. Hybertsen and Steven G. Louie. Electron correlation in semiconductors and insulators: Band gaps and quasiparticle energies. *Phys. Rev. B*, 34:5390–5413, 1986.

[9] Qi-Kang Yin, Chuan-Lu Yang, Mei-Shan Wang and Xiao-Guang Ma. Two-dimensional heterostructures of AuSe/SnS for the photocatalytic hydrogen evolution reaction with a Z-scheme. *J. Mater. Chem. C*, 9:12231-12238, 2021.

[10] Sonali Saha, T. P. Sinha, Abhijit Mookerjee. Electronic structure, chemical bonding, and optical properties of paraelectric $BaTiO_3$. *Phys. Rev. B*, 62:8828–8834, 2000.

[11] Ping Li, Chang-wen Zhang, Jie Lian, Miao-juan Ren, Pei-ji Wang, Xiao-hong Yu and Shang Gao. First-principle study of optical properties of Cu-doped CdS. *Opt. Commun.*, 295:45–52, 2013.

[12] Yafei Li and Zhongfang Chen. Tuning electronic properties of germanane layers by external electric field and biaxial tensile strain: a computational study. *J. Phys. Chem. C*, 118:1148–1159, 2014.

[13] D. B. Melrose and R. J. Stoneham. Generalised Kramers-Kronig formula for spatially dispersive media. *J. Phys. A: Math. Gen.*, 10:L17, 1977.

[14] J. K. Nørskov, J. Rossmeisl, A. Logadottir, L. Lindqvist, J. R. Kitchin, T. Bligaard and H. Jónsson. Origin of the Overpotential for Oxygen Reduction at a Fuel-Cell Cathode. *J. Phys. Chem. B*, 108(46):17886–17892, 2004.

[15] Xuefeng Chen, Wenna Han, Zhizhong Tian, Qian Yue, Chengxiao Peng, Chao Wang, Bing Wang, Huabing Yin, and Qinfen Gu. Exploration of Photocatalytic Overall Water Splitting Mechanisms in the Z-Scheme SnS_2/β-As Heterostructure. *J. Phys. Chem. C*, 127:6347–6355, 2023.

[16] Chongyi Ling, Li Shi, Yixin Ouyang, Xiao Cheng Zeng, and Jinlan Wang. Nanosheet supported single-metal atom bifunctional catalyst for overall water splitting. *Nano Lett.*, 17(8):5133–5139, 2017.

[17] Charles Kittel. *Introduction to Solid State Physics*. 8th edition. John Wiley & Sons, 2004.

[18] Heather M. Jaeger, Sean Fischer, and Oleg V. Prezhdo. Decoherence-induced surface hopping. *The Journal of Chemical Physics*, 137(22):22A545, 2012.

[19] Qijing Zheng, Weibin Chu, Chuanyu Zhao, Lili Zhang, Hongli Guo, Yanan Wang, Xiang Jiang and Jin Zhao. Ab initio nonadiabatic molecular dynamics investigations on the excited carriers in condensed matter systems. *WIREs Comput. Mol. Sci.*, 9(6):e1411, 2019.